

Atmospheric Phase Noise and Aperture-Synthesis Imaging at Millimeter Wavelengths

M. C. H. WRIGHT

Radio Astronomy Laboratory, University of California, Berkeley, California 94720

Electronic mail: wright@creek2.berkeley.edu

Received 1995 May 6; accepted 1996 March 22

ABSTRACT. We analyze data obtained with the Hat Creek interferometer at 86 GHz to estimate the atmospheric phase noise on spatial scales of 6 to 846 m, and time scales of 1 s to 10 hr. We find a phase structure function with a power-law index, β between 0.6 and 1.7. A slope close to the Kolmogorov 2D value 0.67 is obtained for longer baselines and stable weather conditions; the slope approaches the Kolmogorov 3D value 1.67 only on short baselines and in turbulent weather. The rms phase at a 1 km baseline is 1 mm, with a variation by a factor 4 over a few days even during good weather conditions. The mean elevation dependence is $\sin(\text{elevation})^{-0.7 \pm 0.2}$. The variation of β and the elevation dependence with baseline length are consistent with turbulent regions 100–300 m thick. The resolution and dynamic range of millimeter-wavelength aperture-synthesis images is limited by atmospheric turbulence. Observing techniques and data-analysis procedures to correct for atmospheric seeing are discussed in some detail.

1. INTRODUCTION

Atmospheric turbulence creates refractive index variations which limit the resolution and sensitivity of observations of astronomical sources. At optical wavelengths, the seeing is limited by tropospheric density fluctuations with typical size 10 cm, and time scales of 10 ms. At radio wavelengths, the refractive index of water vapor is 20 times larger than at optical wavelengths and fluctuations in the water vapor are more important. At wavelengths longer than 30 cm, fluctuations in the ionosphere limit the resolution. (See Baldwin and Wang 1990, for a recent review of radio seeing, and Masson 1994a, for a comparison of optical and radio seeing.) At millimeter wavelengths, refractive index fluctuations are expected to be dominated by water-vapor variations which are coupled through temperature and relative humidity to the velocity field. Refractive index fluctuations inferred from interferometer phase measurements have been observed with sizes from 1 m to 10 km, and persistence times from 0.1 s to several hours.

The wave front from a radio source is distorted by atmospheric refractive-index variations, which results in phase variations across the telescope aperture. An interferometer array directly observes the path difference through the atmosphere between the two antennas on each baseline. Fluctuations on a larger scale than the antenna separation are partially correlated at each antenna, and the interferometer phase fluctuations are reduced on short baselines.

The phase structure function (PSF), $D\phi(b, T)$, is used to measure the phase fluctuations as a function of the time interval between samples, T , and separation between antennas, b :

$$D\phi(b, T) = \langle [\phi(x, t) - \phi(x + b, t + T)]^2 \rangle. \quad (1)$$

The phase structure function is assumed to be isotropic. For three-dimensional, Kolmogorov turbulence, the structure function follows a power law b^β with a slope $\beta = 5/3$ for

values of b between an outer scale, L , where energy is deposited into the medium, and an inner scale, l , where the energy is dissipated (Kolmogorov 1941). On spatial scales larger than the thickness of the turbulent region, the turbulence is expected to become two dimensional and the structure function scales as $b^{2/3}$ (Tatarskii 1961). Under the Taylor hypothesis, the bulk velocity of the turbulent pattern is larger than the internal velocities, and the time variation follows the same power law with $t = b/v$, where v is the drift velocity of the turbulence past the telescopes (Taylor 1938).

Model atmosphere calculations by Treuhaft and Lanyi (1987) predict a smooth transition from a 5/3 power law at baselines small compared to the scale height of the water vapor, to a 2/3 power law at large antenna separations. The scale height of the water vapor is about 2 km (Thompson et al. 1986); at longer baselines the fluctuations increase slowly with baseline length. On very long baselines, for example in VLBI experiments, the fluctuations are independent of baseline length since the variation with baseline length is not detectable in typical experiments; observations over several days would be required to observe the fluctuations corresponding to the passage of weather systems.

Observations of radio seeing have found a wide range of slopes, β , mostly falling between 2/3 and 5/3, and consistent with the Kolmogorov–Taylor theory. Observations at 5 GHz with the VLA on baselines 1–35 km (Armstrong and Sramek 1982) found $\beta = 1.4$ in reasonable agreement with the Kolmogorov theory for 3D turbulence, although the baselines involved were larger than the scale height of the troposphere, and hence larger than the expected outer scale. More recent analysis of a large set of VLA data at 5 and 15 GHz (Sramek 1990) found a median value $\beta = 0.68$. From an analysis of stellar scintillation, Coulman and Vernin (1991) propose an outer scale as small as 5 m, with a shift from a Kolmogorov 5/3 index, through a “spectral gap” from 5–1200 m, and a Kolmogorov 2/3 index at baselines greater than 1200 m. Ob-

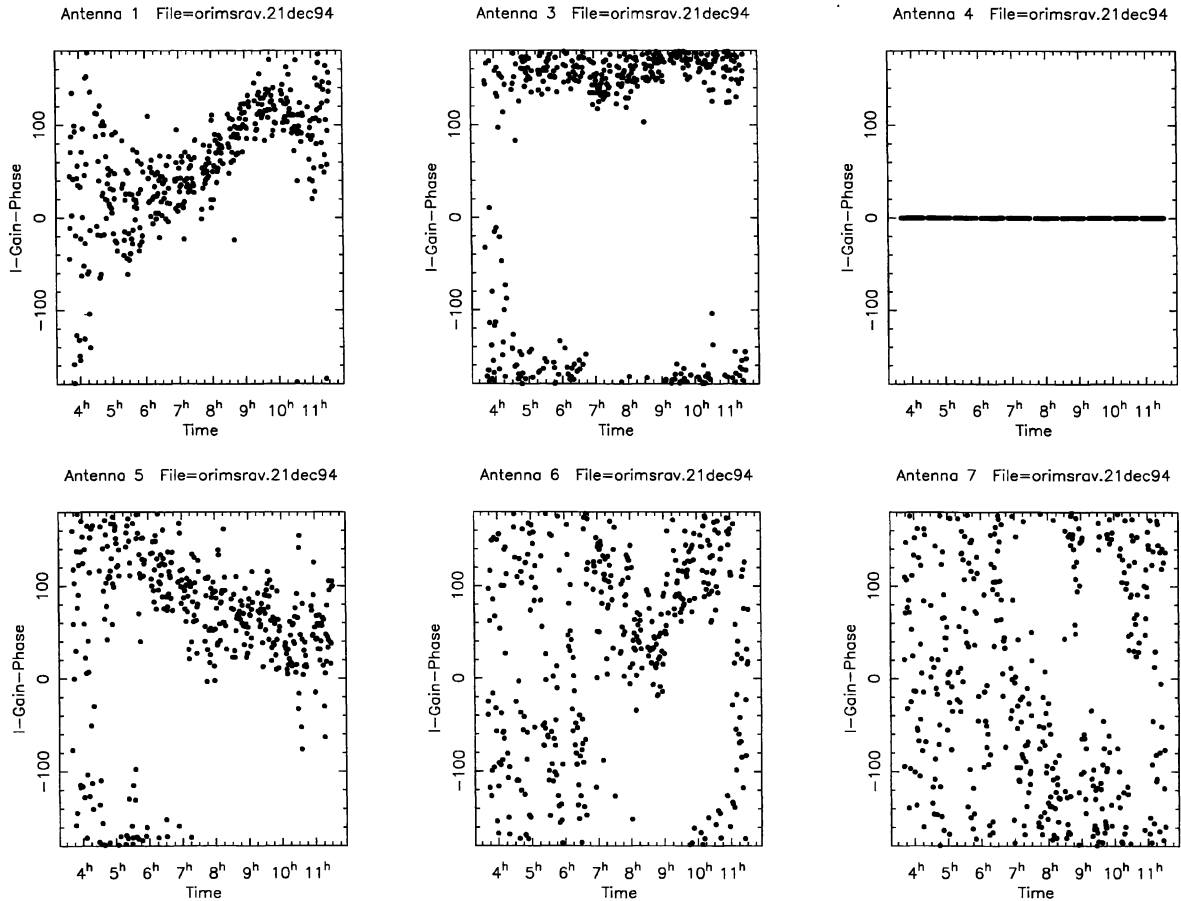


FIG. 1.—The interferometer phase for the Orion SiO maser with antenna separations from 97 to 846 m. The phases are plotted with respect to antenna 4.

servations at $10 \mu\text{m}$ show significant departures from the Kolmogorov model; under good seeing conditions the phase structure function of time is proportional to the time interval—a random-walk process (Bester et al. 1992).

Atmospheric phase fluctuations scale with frequency, and become an important factor in the design and operation of millimeter arrays (e.g., Holdaway 1992a). If uncorrected, phase fluctuations limit the resolution to about 0.5 arcsec at 3 mm wavelength (Bieging et al. 1984), and 1 arcsec at 1 mm (Olm and Downes 1992). Poorer resolution will be obtained at shorter wavelengths since the phase fluctuations scale as $b^{\beta/2}/\lambda$, and hence the seeing limited resolution, scales as $\lambda^{-2/\beta}$ (Thompson et al. 1986). Previous observations at millimeter wavelengths (Bieging et al. 1984; Wright and Welch 1990; Kasuga et al. 1986; Olmi and Downes 1992) covered only a small range of baselines. Until recently, millimeter wavelength aperture synthesis techniques have used the same algorithms developed for centimeter wavelength interferometry, with instrumental gain and phase calibrations at intervals of 15 to 30 min. This procedure has worked quite well for baselines less than about 300 m in good weather conditions, but excessive phase noise at longer baselines, or in less perfect weather requires significantly modified observing and data-reduction techniques. In this paper we analyze data from the BIMA array on time scales of 1 s–10 hr and an-

tenna separations from 6–846 m, and discuss observing techniques and data-analysis procedures to correct for atmospheric seeing.

2. OBSERVATIONS

The observations reported here were obtained with the BIMA 6-antenna array during the period 1993 July to 1995 October. Most of the data are by-products of aperture synthesis observations of the SiO maser emission at 86.243 GHz from OMC1 in one of the standard array configurations with projected antenna separations ranging from 6 to 846 m. (see Wright et al. 1995; Plambeck et al. 1995). These observations are up to 10 hr in length with integration times 10 to 30 s. The SiO maser emission provides a strong signal that clearly differentiates atmospheric effects from instrumental and thermal phase noise. For a single source, errors in the position and instrumental baseline have a 12-hr period and do not contribute to the measured phase noise. Figure 1 shows the interferometer phase for the Orion SiO maser with antenna separations from 97 to 846 m. Fluctuations in the closure phase and in the relative phase of two spectral features centered at -6 and 14 km s^{-1} are less than 1 degree of phase in a 15-s integration, corresponding to $10 \mu\text{m}$ of path length at the line frequency. This is consistent with thermal

TABLE 1
RMS Path (mm) at 1 km and Slope vs. Physical Baseline

Date	5 min		15 min		45 min		135 min	
	sigma	slope	sigma	slope	sigma	slope	sigma	slope
93 Nov 07	0.11	0.36	0.13	0.26	0.26	0.22	0.44	0.14
93 Nov 20	0.21	0.49	0.18	0.32	0.21	0.21	0.62	0.25
93 Dec 25	0.55	0.68	0.63	0.69	0.74	0.66	0.75	0.58
94 Jan 27	0.28	0.41	0.36	0.41	0.49	0.45	0.74	0.58
94 Apr 10	1.31	0.62	1.72	0.66	2.52	0.75	1.79	0.61
94 Dec 14	0.78	0.47	1.09	0.52	1.31	0.44	2.35	0.36
94 Dec 15	0.43	0.30	0.66	0.43	1.03	0.52	2.15	0.69
94 Dec 20	0.89	0.26	1.37	0.35	1.98	0.33	3.27	0.39
94 Dec 21	0.62	0.36	0.86	0.48	1.46	0.62	1.93	0.52
94 Dec 25	0.57	0.43	0.81	0.56	1.27	0.76	1.56	0.63
94 Dec 28	0.82	0.27	1.33	0.38	1.96	0.34	2.17	0.36
95 Jan 01	0.79	0.36	1.12	0.42	1.75	0.48	3.66	0.59
95 Jan 02	0.52	0.40	0.82	0.51	1.59	0.93	2.31	0.73
95 Feb 07	0.53	0.41	0.68	0.43	1.10	0.57	1.80	0.64
95 Feb 08	0.75	0.31	1.18	0.38	1.58	0.38	2.34	0.45
95 Aug 15	2.33	0.64	3.65	0.58	-	-	-	-
95 Aug 17	1.02	0.77	2.69	0.95	-	-	-	-
95 Aug 18	0.66	0.61	0.86	0.51	-	-	-	-

noise from the receiver and atmospheric opacity. The atmospheric phase noise we observed at an 800 m baseline is 100 times the thermal phase noise.

We also made a number of special observations to investigate the atmospheric phase behavior with integration times as short as 1 s, and as a function of source separation, time of year, time of day, wind speed, and humidity. The short integrations were obtained with a fast sampling program designed for solar observing. Most of these observations used a 2-s integration time, giving a sample interval 2.3 s, and a thermal phase noise 3 degrees on 3C273 in an 800 MHz bandwidth. In order to switch between sources as rapidly as possible, we observed a pair of sources as offset pointing positions in a multi-field (mosaicing) observation. In this way we reduced the system overhead to a minimum and were able to alternate between the quasars 3C273 and 3C279 in 30 s, including a 10-s integration on source. These observations were also made with an 800 MHz bandwidth, giving a thermal phase noise of around 1 degree in a 10-s integration.

For each dataset we derived the following quantities: rms phase as a function of baseline length, the Allan deviation, and the temporal spectrum of the phase fluctuations. The total power, air temperature, relative humidity, and wind speed and direction were recorded with most datasets so we were able to investigate the correlations with these parameters.

3. RESULTS

We fitted structure functions of the form

$$\text{rmspath} = \sigma \times \text{baseline}^{\beta/2} \times \sin(\text{elevation})^{-0.5} + \text{noise}, \quad (2)$$

where σ is the intercept at a 1 km baseline, and β is the slope of the phase structure function for sufficiently long averaging times (see Sec. 4.1). The thermal noise from the electronics, antenna spillover, and atmospheric opacity is insignificant compared with the atmospheric phase noise; varying the

noise term from 0 to 10 degrees did not change the results.

For the SiO maser data we computed the rms phase over intervals of 5 to 135 min. The phase was unwrapped from a -180 to 180 degree interval using a simple nearest-neighbor algorithm which was sufficient for this well-sampled, high signal-to-noise data. The best sampled data are listed in Tables 1 and 2. Table 1 shows the fitted rms path at a 1 km baseline, and the slope as a function of the physical baseline length, with the elevation dependence set to $\sin(\text{elevation})^{-0.5}$. For the longer datasets, and for the shorter averaging intervals, we were able to fit for the elevation dependence. These fits are shown in Table 2. We tried fitting versus the projected baseline length (as in Bieging et al. 1984; Wright and Welch 1990; Olmi and Downes 1992), and versus the physical baseline length (as in Sramek 1983; Armstrong and Sramek 1982; Sramek 1990). With a small number of antennas a larger sample of baseline lengths is obtained by fitting versus the projected baseline length rather than the physical baseline length. The choice of baseline variable depends on the atmospheric model. For a thin layer of turbulence, the paths to the antennas are separated by the antenna separations, but for a thick layer the separation is the projected baseline. In fact it does not seem to make much difference to the fitted variables. The best sampled data was obtained in the period 1994 Dec 14 to 1995 Feb 08, with antenna separations from 97 to 846 m, and projected baselines from 60 to 846 m. For these 10 runs the mean value of the rms, σ , and slope, $\beta/2$, in a 5-min interval at a 1 km antenna separation is $\sigma_{5 \text{ min}}(1 \text{ km}) = 0.67 \pm 0.15$, and $\beta/2 = 0.36 \pm 0.07$. Using the projected baseline as the independent variable we obtain $\sigma = 0.82 \pm 0.08$, and $\beta/2 = 0.38 \pm 0.03$. The tighter fit using projected baselines might be construed as evidence against a thin turbulent screen. The rms increases with averaging interval roughly as the 1/3 power; β increases slightly. The mean values for the ten runs are: $\sigma_{15 \text{ min}}(1 \text{ km}) = 0.99 \pm 0.11$, and $\beta/2 = 0.45 \pm 0.07$, $\sigma_{45 \text{ min}}(1 \text{ km}) = 1.50 \pm 0.33$, and $\beta/2 = 0.54 \pm 0.14$. The data are less well sampled

TABLE 2
RMS Path at 1 km, Slope, and Elevation Dependence

Date	5 min			15 min		
	sigma	slope	elevation	sigma	slope	elevation
1993 Nov 07	0.08	0.36	-0.86	0.13	0.26	-0.42
1993 Nov 20	0.15	0.51	-0.74	0.18	0.33	-0.54
1993 Dec 25	0.50	0.71	-0.65	0.63	0.70	-0.58
1994 Jan 27	0.23	0.44	-0.92	0.32	0.44	-0.79
1994 Apr 10	1.38	0.65	-1.13	1.33	0.68	-1.24
1994 Dec 14	0.70	0.46	-0.67	1.06	0.53	-0.55
1994 Dec 15	0.34	0.29	-0.84	0.47	0.40	-0.94
1994 Dec 20	1.37	0.28	0.09	2.12	0.37	0.09
1994 Dec 21	0.36	0.31	-1.19	0.39	0.38	-1.51
1994 Dec 25	0.42	0.43	-1.01	0.56	0.45	-0.88
1994 Dec 28	0.83	0.27	-0.48	1.36	0.38	-0.47
1995 Jan 01	0.82	0.36	-0.44	1.23	0.44	-0.38
1995 Jan 02	0.32	0.37	-1.27	0.52	0.47	-1.27
1995 Feb 07	0.62	0.43	-0.29	0.81	0.45	-0.28
1995 Feb 08	1.27	0.34	0.32	1.95	0.42	0.27

for the other data included in Table 1, and the range of baselines is smaller (6 to 52 m in 1993 November 12 to 128 m in 1993 December 31, to 238 m in 1994 January, and 12 to 83 m in 1995 August). However, as is evident from Tables 1 and 2, smaller values of σ were obtained in the winter of 1993, and much larger values in summer than in winter. The mean values for the winter (October to March), and summer (April to September) are: $\sigma_{15 \text{ min}}(1 \text{ km})=0.80 \pm 0.40$, and $\beta/2=0.44 \pm 0.11$, and $\sigma_{15 \text{ min}}(1 \text{ km})=2.23 \pm 1.21$, and $\beta/2=0.67 \pm 0.19$, respectively. The rms phase noise can change by a factor 2 to 3 in a few days. Although the values for σ and β are inversely correlated in the fits (a high β can compensate for a low σ , and vice-versa), in the best conditions we obtain a low value for both σ and β ; in the worst conditions both σ and β increase.

We investigated the correlation of σ and β with humidity and wind speed. Outside of the seasonal variation, there is little correlation of either σ or β with humidity. There is a significant correlation of both with wind speed, which is most evident in typical summer afternoon conditions at Hat Creek. Quantitatively, we have measured a 50% increase in phase noise for a wind increase from 2 to 6 m s⁻¹, and an increase in β to 1.7, on baselines less than 40 m. We have found little correlation with the wind direction.

For the source switching data we analyzed whether the rms phase in one source could be reduced by interpolating the phase from the other. These results are discussed in more detail below.

To verify that the fitted parameters were not generated by some quirk of data sampling or software, we generated several sets of interferometer data with similar sampling to the real data, but with the data replaced by Gaussian additive (thermal) noise, or with Gaussian phase noise, or both. In all cases the result of computing phase-structure functions, Allan deviations, and power spectra was to produce zero slopes as a function of baseline, time, or frequency, respectively.

4. DISCUSSION

4.1 Phase Structure Function

An interferometer array directly measures the PSF over the range of baselines in the array, without invoking Taylor's hypothesis. The data must be averaged over sufficient time to sample the full range of the fluctuations; usually stated as a few times b/v , where b is the antenna separation, and v the wind velocity. In practice, turbulence is experienced even in extremely low winds, and instrumental phase drifts can increase the measured fluctuation if the interval is too long. Only a mean value was removed in computing the PSF. As noted by Sramek (1990), removing a slope risks lowering the measured turbulence. The largest errors in the values listed in Tables 1 and 2 come from instrumental phase drifts. Instrumental phase drifts due to cable length variations are removed from the data. However, there was a problem with phase drifts on the long baselines which becomes apparent at the longer integration times in Table 1. Instrumental phase drifts on the short baselines were much better controlled. Removing a linear phase slope from the data reduces both the rms and the fitted slope. For averaging times less than 45 min, the changes are typically 2–5 percent in σ , and 5–10 percent in the slope. For an averaging time of 135 min, σ decreases by up to 10 percent and the slope by as much as 25 percent which is probably an upper limit to the systematic errors. The agreement of the rms derived from the PSF and Allan deviation, which removes a linear phase slope from the data, suggests that instrumental phase drifts are not a problem for shorter averaging times.

The averaging time is an important parameter. If one were only interested in the atmospheric statistics, then longer averaging times are required on longer baselines. However, the astronomer is more likely to be interested in how the phase varies with baseline for a fixed averaging time. The PSF provides an estimate of the error in the measured phase after a calibration interval corresponding to the averaging time. Tables 1 and 2 list the rms phase for various averaging times.

TABLE 3
Published Structure Function Measurements

Baseline	Frequency [GHz]	rms path [mm]	Slope [β]	Reference
1.6 km	5	0.7–2.6	1.3	Hinder and Ryle (1971)
1–35 km	5	1.0	1.4	Armstrong and Sramek (1982)
100 m–3 km	22	0.6	0.72	Sramek (1983)
12–150 m	86	1.2	1–2	Bieging et al. (1984)
27–540 m	22	0.5–0.9	1.6	Kasuga et al. (1986)
50 m–35 km	5/15	0.6–1.6	0.6–0.8	Sramek (1990)
35 m	19	1.9	1.2	Ishiguro et al. (1990)
6–100 m	86	0.7–1.0	1.1–1.4	Wright and Welch (1990)
1–1200 km	100	0.7	0.3–0.6	Wright and Welch (1990)
24–288 m	86	0.3–0.7	1.1–1.9	Olimi and Downes (1992)
100 m	12	0.2–1	0.4–2	Masson (1994)
6–846 m	86	0.8–2.2	0.8–1.3	This paper

Fixed averaging times will tend to underestimate β for the shorter averaging times. Indeed, the measured slope of the PSF does increase slightly with averaging interval.

The standard instrumental phase calibration at an interval of 15–30 min suppresses fluctuations on longer time scales, and we will adopt 15 min as a standard averaging interval, in common with several recent studies. Published measurements of PSFs are summarized in Table 3. The measured phase noise has been converted to an rms path length at a 1 km baseline, using the β given in Table 3. The published phase noise and β are generally consistent with an rms path around 1 mm at a 1 km baseline. The rms path ranges over an order of magnitude from 0.2 to 4 mm. (Observers usually do not publish their worst data, so 4 mm is a lower limit.)

The fitted power-law slope, β , varies from 0.3 to 2, with the steeper slopes generally on the shorter baselines. Plots showing this trend from 2D to 3D turbulence (Wright and Welch 1990; Masson 1994a), suggest that the break occurs around 100 to 300 m. The break is not readily apparent in any of our data (see, e.g., Fig. 3), but if we fit the best sampled datasets between 1994 Dec 14 and 1995 Feb 08 we obtain an average $\beta=1.16\pm0.06$ for baselines less than 300 m (the median value); while for baselines between 300 and 846 m we obtain $\beta=0.48\pm0.10$. This result, using a 15-min averaging interval may underestimate β on the long baselines. Using a 45-min averaging interval, we obtain an average $\beta=1.18\pm0.21$ for baselines less than 300 m, and $\beta=0.58\pm0.10$ for baselines between 300 and 846 m. The two studies with the largest slopes (Armstrong and Sramek 1982; Olmi and Downes 1992) both used array baseline data comprised of several widely separated sources sampled for short intervals. The three-dimensional nature of the sampling may result in a high β close to the Kolmogorov 3D value 5/3. Alternatively, the VLA data at 5 GHz (Armstrong and Sramek 1982) may also suffer from ionospheric fluctuations which are readily apparent in VLBI data up to 10 GHz (Thompson et al. 1986), and $\beta=1.4$ on Plateau du Bure at 86 GHz (Olimi and Downes 1992) is consistent with the relatively short baselines sampled. On longer baselines, and in good weather, β tends toward 0.7, consistent with that expected for 2D Kolmogorov turbulence. A stable atmosphere over level ground is horizontally stratified with a capping inversion which varies in height from about 100 m at night to

1–2 km by day (e.g., Kaimal and Finnigan 1994). Most of the turbulence is expected to be within this Planetary Boundary Layer (PBL) (Panofsky and Dutton 1984), although mixing through the capping inversion has been cited (Coulman 1991) as a possible mechanism for creating the large, anomalous refraction observed on radio telescopes at Pico Veleta (Altenhoff et al. 1987), and on Mauna Kea (Church and Hills 1990). A 10'' refraction fluctuation observed with the JCMT telescope on Mauna Kea corresponds to a 0.75 mm path gradient across the 15-m telescope; this is much larger than the fluctuations typically observed with interferometers on a 15 m baseline. The large “anomalous” refractions correspond to the peak phase fluctuations seen in poor observing conditions at Hat Creek. As noted by Altenhoff et al. (1987), the more typical refraction fluctuations of 1''–2'' are consistent with the path-length variations seen with interferometers.

Additional evidence for a thin turbulent layer or layers comes from the observed elevation, dependence. For three-dimensional turbulence the rms phase should scale approximately as $\sin(\text{elevation})^{-0.5}$, for two-dimensional turbulence, as $\sin(\text{elevation})^{-1.0}$. For the ten well-sampled datasets between 1994 Dec 14 and 1995 Feb 08, we obtain an average elevation index 0.67 ± 0.20 for baselines less than 300 m, and 0.80 ± 0.22 for baselines between 300 and 846 m.

There is little direct evidence for a cutoff in the slope, even on baselines to 35 km (Sramek 1990), and the rms phase continues to increase slowly to VLBI baselines (Wright and Welch 1990). On baselines longer than the scale height of the water vapor, the dry atmosphere may contribute to the measured phase fluctuations. From an analysis of phase fluctuations in VLBI data, Rogers (1988) suggests that up to 30 percent of the fluctuations are from the dry component. There may also be a significant amount of turbulence in the upper atmosphere, perhaps associated with the diurnal breakup of the PBL, or with weather fronts (see, e.g., Coulman 1991).

On short baselines or in turbulent weather, β approaches the Kolmogorov 3D value of $\beta=5/3$. This case corresponds to summer afternoon conditions at Hat Creek when there are strong vertical thermal gradients, as evidenced by (latent) thunder-storm activity, and winds 5 to 10 m s⁻¹. Only in these conditions do we observe the Kolmogorov value 5/3.

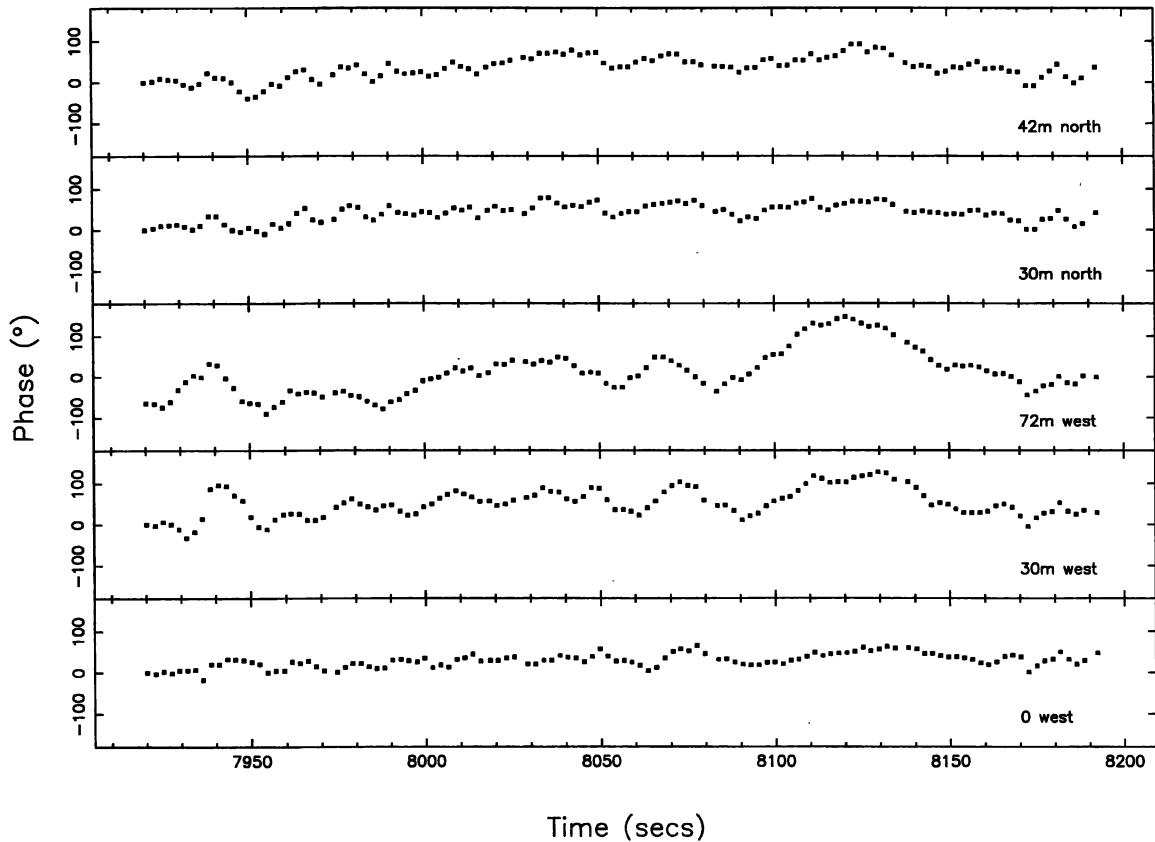


FIG. 2—This shows a well-defined atmospheric phase event during a short run of data on the Orion SiO maser sampled at 2.3-s intervals on 1995 July 28. The antennas are located at 0, 30, and 72 m west, 30, and 42 m north, respectively, with respect to a reference antenna at 12 m east.

4.2 Taylor's Hypothesis

Taylor's hypothesis (Taylor 1938) allows us to infer spatial structure from the temporal structure measured at one point, assuming that the turbulent pattern is frozen as it is blown across the array at the mean wind velocity. This powerful assumption allows us to compute the spatial PSF directly from the temporal PSF, and has been used, for example, to predict the PSF expected on prospective MMA sites from observations of water-vapor temporal fluctuations (Holdaway 1991). Support for Taylor's hypothesis comes from the consistency of the spatial and temporal statistics of wind fluctuations (Kaimal and Finnigan 1994). From an analysis of the cross correlation of data obtained with the Cambridge One Mile Telescope, Hinder (1972) found agreement with Taylor's hypothesis; in 80 percent of the data he analyzed, the phase fluctuations were consistent with a turbulent pattern crossing the 3-antenna array with the wind velocity, the remaining 20 percent were not consistent with frozen turbulence. However, turbulence is neither frozen, nor transported at a uniform velocity. Many an unlucky sailor has watched a favorable gust crossing the water, only to find that it has rearranged itself by the time it reaches his, or her, boat. We looked for evidence of coherent structures crossing the Hat Creek array. There is no apparent difference in the magnitude or frequency of the fluctuations parallel and per-

pendicular to wind, although the statistics obtained with a 6-antenna array are rather poor. The wind speed may increase above the surface layer 50–100 m deep, but the direction is maintained over level ground (see, e.g., Kaimal and Finnigan 1994). Figure 2 shows a short run of data on the Orion SiO maser sampled at 2.3-s intervals on 1995 Jul 28. The data were obtained in clear weather with wind speed 2 to 4 m s⁻¹ from a direction 220 to 240 degrees. The rms phase is well fitted to $b^{0.8}$. The phase fluctuations are correlated across the array, but are not delayed in the wind direction as might be expected if there were a frozen turbulent pattern being blown across the array. A cross-correlation analysis of the phase fluctuations shows multiple peaks, perhaps indicating several layers of frozen turbulence moving past the antennas at different velocities, but our data do not offer much support for the Taylor hypothesis. The anisotropy of the temporal phase fluctuations across the array favors a more isotropic distribution of velocity fluctuations. Studies of the transport velocities of turbulent eddies (Wilczak and Businger 1984) show that large eddies move faster than small eddies, and that the average transport velocity is 0.7 to 0.8 times the mean wind velocity. In a convective atmosphere, or over hilly terrain, the vertical wind speed may exceed the horizontal component. Standing waves and strong wind shears (gradients) are not compatible with Taylor's hy-

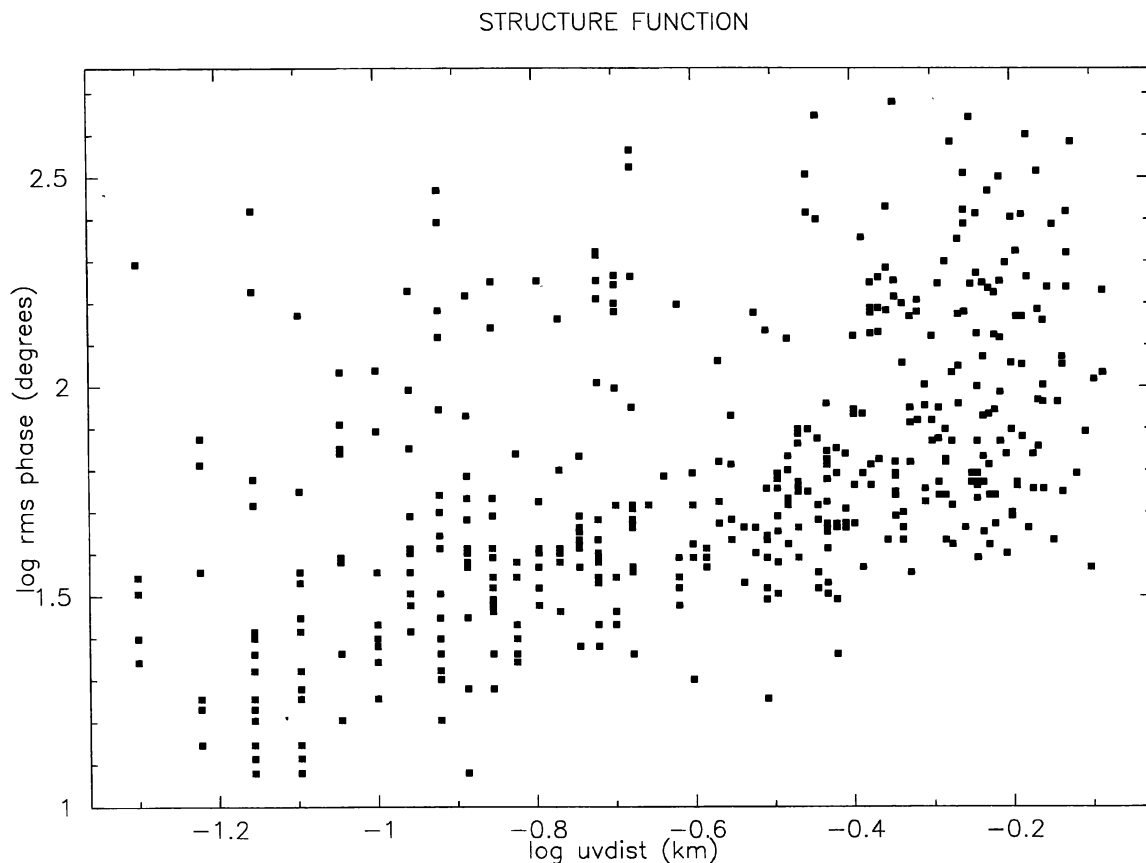


FIG. 3—The phase structure function for 1994 December 21. Each point represents a 15 min sample of the data from which an rms phase was calculated.

pothesis, which fails, for example, if the vertical wind shear, du/dz is greater than u/b , where u is the mean horizontal wind velocity, and b is the antenna separation.

On average there is a net transport of water vapor from the surface in order to balance precipitation. Turbulent eddies mix more humid air close to the surface with drier air above, and carry water vapor, and its latent heat energy, to higher altitudes. Much of the heat flux is transferred by convective plumes of hot air with diameters 100 m (Kaimal 1974); these do not satisfy Taylor's hypothesis (Davison 1974). The water vapor is not well mixed with the dry component; large fluctuations can occur and are the probable cause of the anomalous refraction observed on Mauna Kea (Church and Hills 1990).

Even if turbulence is not "frozen," the statistics of spatial and temporal fluctuations in the water vapor are coupled to those of the wind turbulence. In the analysis below we will assume Taylor's hypothesis is true in a statistical sense, i.e., $\langle b^2 \rangle = \langle (vT)^2 \rangle$, rather than $b = vT$, strictly proportional to the wind speed and direction, and we use the measured horizontal wind as indicative of the transport speed independent of direction. Table 4 lists the predicted slopes of various statistics for Kolmogorov-Taylor turbulence.

4.3 Allan Deviations and Phase Power Spectra

In Table 5 we compare the measured slopes for the PSF and Allan deviation for the best sampled data in the period

1994 Dec 14 to 1995 Feb 08. The PSF was computed for 15-min intervals averaged over all the data. The Allan deviation was derived from $\sqrt{\langle [\phi(t-T) - 2\phi(t) + \phi(t+T)]^2 \rangle}$ averaged over each baseline for a time interval T . The Allan deviation removes linear phase drifts from the data. Figure 4 shows the Allan deviation for 1994 Dec 21. The slope of the Allan deviation flattens at a time, T' , 120 to 1300 s. This "corner time" corresponds to the time for the turbulence to cross the baseline and is directly related to the "corner frequency" discussed by Masson (1994b). The measured corner times are commensurate with the baseline length and average wind speed, 2.2 m s^{-1} , but do not correlate in detail with the baseline and the wind speed, and no accounting has been attempted for wind direction, since similar corner times were seen independent of the measured wind direction with

TABLE 4
Predicted Slopes for Kolmogorov-Taylor Turbulence

Statistic		3D turbulence	2D turbulence
3D spatial power spectrum	α	3.67	2.67
Structure function [β]	$\alpha-2$	1.67	0.67
Temporal phase spectrum	$1-\alpha$	-2.67	-1.67
Allan deviation	$0.5 \alpha-2$	-0.17	-0.67
RMS from time series	$0.5 \alpha-1$	0.83	0.33

TABLE 5
Comparison of Slopes Derived from Phase Structure Function and Allan Deviation

Date	Structure function	Allan deviation	Comment	Wind speed [m s ⁻¹]
1994 Dec 14	0.52	0.50	break at 200 s	1.52 (0.95)
1994 Dec 15	0.43	0.50	break at 150 s	1.75 (1.29)
1994 Dec 20	0.43	0.40	break at 500 s	0.93 (0.85)
1994 Dec 21	0.48	0.50	break at 120 s	1.05 (0.94)
1994 Dec 25	0.56	0.35	break at 700 s	1.31 (1.23)
1994 Dec 28	0.38	0.40	break at 1300 s	6.49 (4.09)
1995 Jan 01	0.42	0.42	break at 400 s	2.68 (2.10)
1995 Jan 02	0.51	0.45	break at 200 s	0.88 (0.77)
1995 Feb 07	0.43	0.45	break at 630 s	1.33 (0.91)
1995 Feb 08	0.38	0.34	break at 800 s	4.53 (1.91)

respect to the baseline orientation. The Allan deviation is a convenient measure of the coherence time for the interferometer, and sets an effective limit to the coherent integration time which can be used to avoid reducing the amplitude in the averaged data (see, e.g., Rogers et al. 1984). The Allan deviation is commonly used to measure the fractional frequency stability of oscillators, $\delta f/f$. The Allan variance of the frequency stability, $\sigma_y(T)^2$, estimated from our atmospheric phase fluctuations is: $1/[2(\pi f T)^2] \langle [\phi(t-T) - 2\phi(t) + \phi(t+T)]^2 \rangle$, where f is the observing frequency,

and T is the time interval, and assuming that the sampled data are contiguous (no dead time). The rms phase over a time interval, T is given by: $\sigma_A(T) = \sqrt{(2)\pi f T \sigma_y(T)}$. The slope of $\sigma_A(T)$ is listed in Table 5. The average slope, for times, T , less than the corner time is 0.43 ± 0.02 , in good agreement with the average slope of the PSF, $\beta/2 = 0.45 \pm 0.02$, but there is not a good correlation in detail, offering support for the Taylor hypothesis in a statistical sense only. The slope of the Allan deviation, defined above, is -0.57 for times less than the corner time. A similar slope is seen in

ALLAN DEVIATION

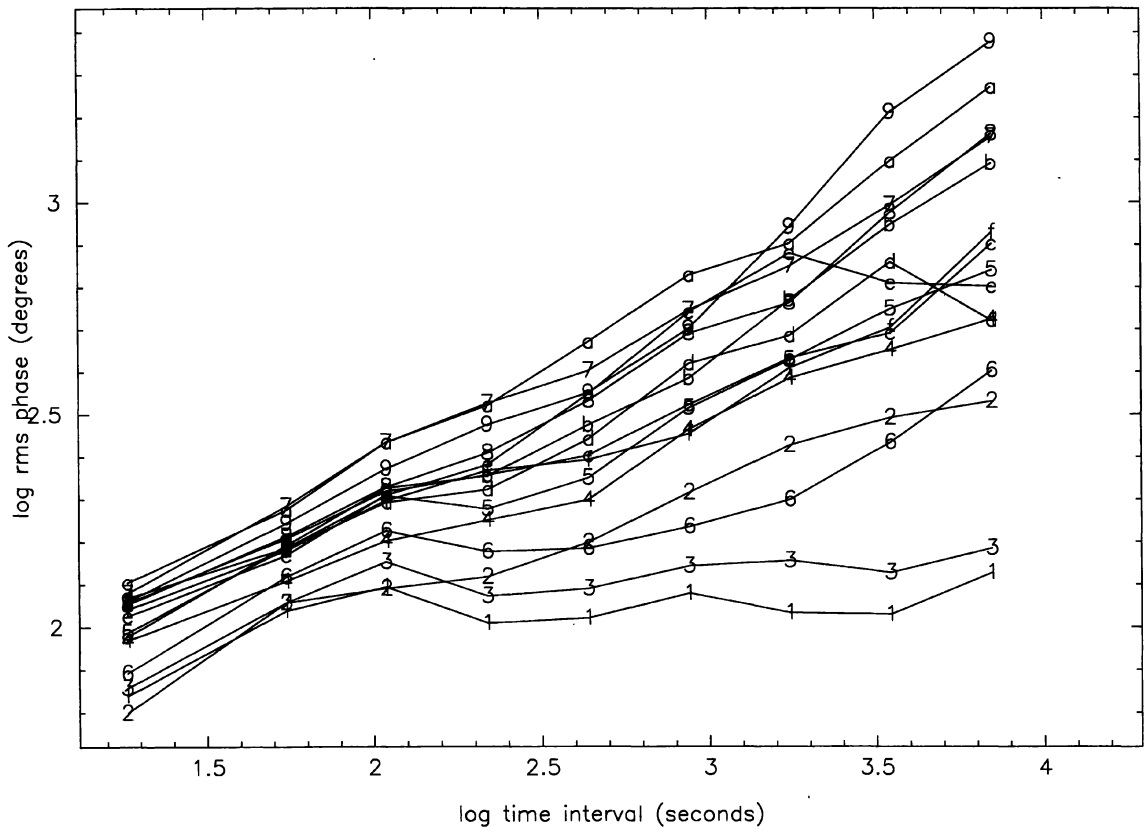


FIG. 4—The Allan deviation for 1994 December 21. The curves show the variation of the rms phase as a function of the time interval between sampled points. The points for each baseline are connected and identified as follows: (1) 70 m, (2) 140 m, (3) 80 m, (4) 160 m, (5) 110 m, (6) 160 m, (7) 260 m, (8) 330 m, (9) 400 m, (a) 370 m, (b) 460 m, (c) 520 m, (d) 580 m, (e) 600 m, (f) 240 m.

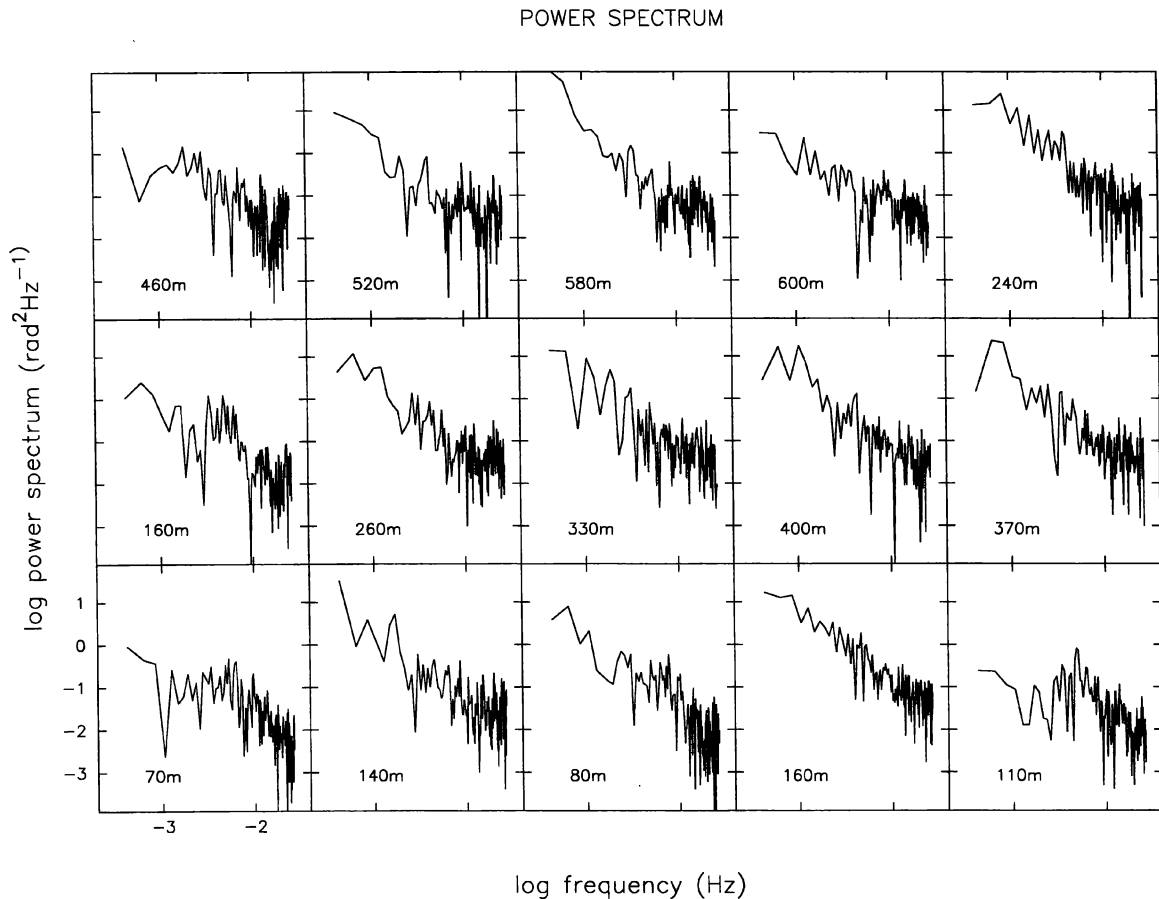


FIG. 5—Temporal phase power spectra for 1994 December 21. Each panel plots the power spectra for contiguously sampled data. The projected baseline length is indicated for each panel.

3-mm VLBI data for averaging times 2 to 500 s (Rogers et al. 1984). The slopes of the PSF and Allan deviation correspond to a spatial-phase spectrum with index $=2.90 \pm 0.06$, and 2.86 ± 0.06 , respectively, close to that expected for 2D turbulence (Tatarski 1961; Armstrong and Sramek 1982).

The phase power spectra were derived from Fourier transforms of contiguous data in each dataset. Each baseline was analyzed separately. A sample of the power spectra obtained on 1994 Dec 21 are plotted in Fig. 5. A flattening of the spectra below a corner frequency ν/b is apparent in some baselines corresponding to the time for fluctuations to cross the array. The low-frequency fluctuations which are evident probably result from uneven sampling and phase drifts in the data over a period of hours. The slope of the spectra above the corner frequency varies widely from about -1.2 to -2.1 , with an average value -1.5 ± 0.2 . The corresponding spatial-phase spectral index 2.5 ± 0.2 is somewhat flatter than that derived from the PSF and Allan deviations. The difference can be understood in terms of the different transport velocity for large- and small-scale turbulence. Since large eddies move faster than small eddies, there is more power in fast time variations than would be expected if the turbulence was frozen.

4.4 Correlations with Time, Weather, and Site

4.4.1 Seasonal, Diurnal

We observe both seasonal and diurnal variations in both σ and β . The increase in σ in daytime (versus night), and summer observing is well known. We also observe an increase in β in conditions of high turbulence. The mean values for the winter (October to March) and summer (April to September) are: $\sigma_{15 \text{ min}}(1 \text{ km})=0.80 \pm 0.40$, and $\beta=0.88 \pm 0.22$, and $\sigma_{15 \text{ min}}(1 \text{ km})=2.23 \pm 1.21$, and $\beta=1.34 \pm 0.38$, respectively. Our statistics for diurnal variation are poor, but a diurnal variation in β was also noted at Plateau de Bure; at night $\beta=1.11 \pm 0.02$, and by day $\beta=1.85 \pm 0.04$ (Olimi and Downes 1992). An increase in β is also suggested by the VLA data: summer daytime $\beta=0.84$, nights= 0.74 , winter days= 0.60 , nights= 0.58 (see Sramek 1990—Table 1). The increase in turbulence is associated with an increase in the depth of the turbulent eddies, and hence in β .

4.4.2 Weather

At Hat Creek we see an increase in both σ and β in turbulent weather, which may be excited by heat input, or by wind. (It is not clear from our data whether the wind stirs up

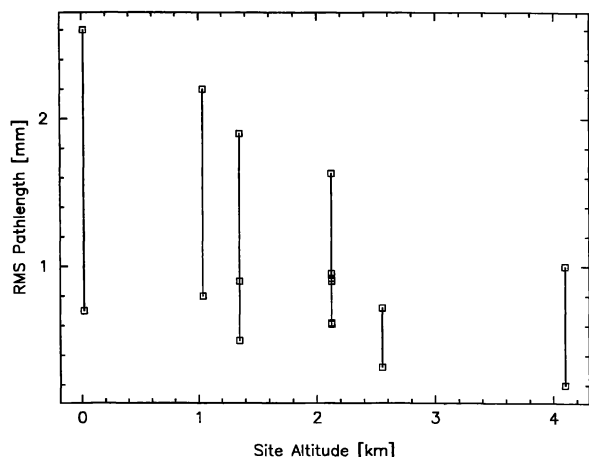


FIG. 6—RMS path length vs. site altitude. A range of values is plotted corresponding to winter and summer averages (Cambridge—17 m; Hat Creek—1035 m; Nobeyama—1350 m), winter and summer, day and night (VLA—2124 m), night and day (IRAM—2550 m), and for a range of β (Mauna Kea—4100 m). References as in Table 3.

larger eddies, or heat input creates both larger eddies, and stronger winds.) An increase in the humidity does not by itself lead to an increase in σ . At Cambridge, Hinder (1972), noted a correlation of σ with temperature (correlation coefficient, $\rho=0.58$), with duration of sunshine ($\rho=0.46$), and with cloud cover ($\rho=-0.51$), but no correlation with wind speed ($\rho=0.00$). These results suggest that increased phase fluctuations are associated with convective activity.

4.4.3 Site Altitude and Topography

The best rms path reported to date (Masson 1994b) is at the highest altitude (4100 m), and a general decrease in the average values of σ with site altitude is evident in Table 3. In Fig. 6 we plot σ versus site altitude, extrapolating to a 1 km baseline using the published values of β . Better statistics for the variation of σ with altitude have been recently reported by Holdaway (1995) using satellite observations at 10 to 12 GHz on a 150–300 m baseline at Nobeyama, Mauna Kea, and Chile. The data are consistent (with the usual caveats about extrapolating to longer baselines and millimeter wavelengths) with a decrease in σ with altitude, which is more shallow than the decrease in the total path—suggesting that the turbulent water vapor is in active layers, and not distributed though the total path; most likely at the top and bottom of the PBL (Lewellen 1980).

A high altitude does not guarantee a low σ ; 10'' pointing errors due to anomalous refraction observed on Mauna Kea (Church and Hills 1990) correspond to path-length changes of 1 mm over a distance of only 20 m. Moreover these large fluctuations can occur under conditions of low humidity, less than 1 mm of precipitable water vapor, or 6 mm of total path due to water vapor. Clearly, very large fractional fluctuations are possible under some conditions. The rms path is a larger fraction of the total path at higher altitudes. In the case of the anomalous refraction reported at Pico Veleta at 2850 m altitude (Altenhoff et al. 1987), and at JCMT at 4100 m altitude

(Church and Hills 1990), the fluctuations require that a large fraction of the water vapor be in the form of a gradient, or wedge, over the telescope which causes the observed pointing errors. At the highest altitudes there is insufficient water vapor to support large rms fluctuations in stable atmospheric conditions. The site topography is also important. We might expect that some fraction of the turbulence in the water vapor is injected into the PBL from ground effects (see, e.g., Kaimal and Finnigan 1994). The atmospheric phase fluctuations will then depend on the details of the array configuration and the local topography; there is increased turbulence, for example, in the lee of a hill, and the highest wind velocities are experienced at the crest of a hill. Certainly we might expect more variations in the phase fluctuations measured across the complex topography of Mauna Kea than across a large open site such as the VLA, or the proposed MMA site in Chile. Taylor's hypothesis may be more valid on a large open site (large compared to the size of the telescope array) than in hilly terrain.

4.5 Atmospheric Phase Correction

Methods to correct for atmospheric phase fluctuations can be divided into two classes: (1) direct measurement of the phase shift along the same or adjacent path through the atmosphere; (2) measurement of some related quantity such as the water vapor, or total-power variations along a line of sight to, or close to the source. Several methods have been explored, and are discussed at length by Holdaway and others (1992a, 1992b, 1995). In the following formulation we do not assume that the turbulence is frozen, since there is little direct evidence for this in our data; rather we assume that both the spatial structure and the temporal variations can be described by a phase structure function, with the spatial and temporal variations adding in quadrature.

4.6 Standard Phase Calibration

The standard calibration technique is to alternate observations of the source with short observations of a nearby quasar or other compact source at intervals of 5 to 50 min in order to calibrate the instrumental phase versus time. The phase of the calibrator is interpolated and subtracted from the measured source phase. This calibration corrects for a slowly varying instrumental phase offset, and reduces geometrical errors, Δb , by $\Delta b \cdot (s - s_0)$, where s and s_0 are unit vectors in the directions of the source and calibrator, respectively. The choice of calibrator and calibration interval is a compromise between SNR and calibration errors (e.g., Wright 1991); a stronger calibrator will give better SNR in a shorter interval, but the stronger calibrator is typically located further from the source, resulting in larger geometric errors. The standard calibration also reduces the slowly varying part of the atmospheric phase fluctuations. The effective distance between the source and the calibrator is given by $d = \sqrt{[h(s - s_0)]^2 + (v\Delta T)^2}$, where h is the height of the turbulence in the direction of the source, and v the mean turbulent velocity over an interval ΔT . Both source and calibrator suffer atmospheric phase fluctuation given by the phase structure function $D\phi(b) = \langle [\phi(x+b) - \phi(x)]^2 \rangle$, where b is

the interferometer baseline. After calibration, the phase fluctuations will be reduced if $d < b$. This analysis is similar to that presented by Holdaway (1992b), but does not assume a frozen turbulence drifting past the antennas.

Consider the following examples. Assume $h = 2$ km, a source-calibrator separation = 10 degrees, $v = 10$ m s⁻¹, and $\Delta T = 15$ min. These parameters imply $h(s - s_0) = 350$ m and $v\Delta T = 9$ km. Thus standard calibration will not reduce atmospheric phase fluctuations on baselines less than about 9 km. To reduce the atmospheric phase fluctuations on shorter baselines, a shorter calibration interval should be used. The situation is improved if the velocity of the turbulence is smaller, say $v = 1$ m s⁻¹. In these conditions, and with a shorter calibration interval, $\Delta T = 5$ min, $v\Delta T$ is 300 m, comparable to the term $h(s - s_0)$, then atmospheric phase fluctuations will be reduced on baselines longer than about 460 m. An additional improvement is expected if the turbulence is closer to the antennas, i.e., h is smaller.

4.7 Fast Switching

Atmospheric phase fluctuations can be reduced by rapidly switching between the source and a nearby calibrator. The effect has been nicely demonstrated at the VLA site using a source-calibrator separation of 2 degrees, and a switching time of 40 s. The residual phase fluctuations after calibration increased with baseline to about 400 m, and then remained constant (Holdaway and Owen 1995). Using the above analysis, this is consistent with a mean turbulent velocity of about 7 m s⁻¹. Holdaway and Owen assume Taylor's hypothesis, and derive 10 m s⁻¹. At Hat Creek, we made several tests of fast switching between the bright quasars 3C273 and 3C279, with angular separation 10.4 degrees.

In summer conditions (1994 August and 1995 July), when the atmospheric turbulence is extremely high, the data are consistent with an increase in rms phase on short baselines ($d > b$), and a reduced rms on long baselines ($d < b$) after calibration. For the 1995 July 28 data, with baselines ranging from 8 to 86 m, using 3C273 to calibrate 3C279 with a 30-s switching interval (including a 10-s integration on one source), reduced the fitted PSF slope from 1.5 (close to the Kolmogorov 3D value) to 0.6. The fitted rms phase at a 1 km baseline was reduced from 387 to 111 degrees. The rms phase on baselines less than about 50 m was increased after calibration; on baselines 50–86 m, the rms phase was only slightly reduced, but an improvement by a factor of more than 3 would be obtained at 1 km because of the flatter slope. Using a calibration interval longer than 60 s increased the phase noise on all baselines. The flattening of the phase structure function between 50 and 100 m is consistent with upper limits to the turbulence height and velocity of about 500 m, and 1–2 m s⁻¹, respectively. Using the actual measured wind velocity (4 ± 1 m s⁻¹), we would expect to see a constant rms phase on baselines longer than about 100 m. Unfortunately, our longest baseline in summer was 86 m. In winter, with baselines to 800 m, a repeat of these fast-switching experiments did not lead to the expected improvement on longer baselines. Evidently the atmospheric conditions may vary considerably; the winter experiments imply that $d = \sqrt{(0.18h)^2 + (30v)^2}$ was greater than 800 m. In sum-

mer, the strong thermal gradients create considerable ground-level turbulence, and it is reasonable to expect that much of the turbulent water vapor is close to the ground and can be calibrated by switching to a nearby calibrator on 30-s time scales. In winter, most of the turbulence may be higher and moving faster and is not removed on 30-s time scales. Further experiments are needed with faster switching and closer calibrators. There is a compromise between a weak calibrator close to the source, and a more distant, stronger calibrator which could allow a faster switching cycle. Analysis of atmospheric phase fluctuations in Hat Creek baseline data shows that the rms does not increase rapidly with source separation, suggesting that much of the atmospheric turbulence is close to ground, with h less than about 300 m. A similar result was obtained at the VLA by Sramek (1983) for source-calibrator separations 6–23 degrees. Analysis of radiometer opacity fluctuations at South Baldy (altitude 3200 m) (Holdaway 1991) also suggest that the phase structure function has a turnover at a few hundred m, suggesting that the turbulent layer is only a few hundred m thick.

Clearly, faster switching is desirable. Our fast sampled data show phase fluctuations on 1-s time scales. The switching speed is limited by both hardware and software. At Hat Creek the measured resonant frequency of the antennas is 3–4 Hz in both azimuth and elevation axes. An efficient slew over a few degrees can be achieved in 3–4 s, but the data-acquisition software currently limit the minimum switching time to about 30 s, with a 10-s integration on source.

4.8 Self-Calibration

In self-calibration we estimate the complex antenna gains (amplitude and phase) at each antenna, g_i , from a model of the source visibilities, v_{ij} , by minimizing $\sum_{ij} [(g_i g_j v_{ij} - v'_{ij}) / \sigma_{ij}]^2$ over time intervals ΔT . The model visibilities are usually obtained iteratively from an image of the source distribution (e.g., Cornwell and Fomalont 1989). The estimated antenna phases, including atmospheric phase fluctuations on time scales greater than ΔT , are used to correct the data and make a better image. The conditions for convergence, and the noise introduced into the image by the errors in the estimated antenna phases are discussed by Cornwell and Fomalont. The noise in the estimated gains depends on ΔT . If ΔT is too small then the image quality is limited by the errors, σ_G , in the estimated antenna gains; if ΔT is too long then the image quality is limited by atmospheric phase fluctuations. The optimum self-calibration interval depends on the source flux density and baseline length. Cornwell and Fomalont show that σ_G is approximately $\sigma_v / (S\sqrt{N})$ where σ_v is the thermal noise on each baseline, S is the source flux density, and N the number of antennas. The atmospheric phase noise in an averaging interval ΔT increases with ΔT up to a maximum given by the phase structure function, $D\phi(b)$. The thermal noise decreases as $\sqrt{(\Delta T)}$. The optimum self-calibration interval is obtained where the phase noise from the estimated gains and from the atmosphere are equal. The atmospheric phase fluctuations, after self-calibration, are given by $D\phi(d)$, where d is the rms value of $(v\Delta T)^2$ over the self-calibration interval ΔT and v is the

mean velocity of the turbulence. Atmospheric phase fluctuations on baseline b will be reduced if $v\Delta T$ is less than about $4b$.

At millimeter wavelengths, several spectral lines can often be observed simultaneously. The source structure can change, both within one spectral line as a function of frequency, and also from one spectral line to another. Since the source flux density may be distributed over many channels, a multichannel model is required in the self-calibration. The instrumental frequency response must be calibrated, and removed from the data before a multichannel self-calibration, or before applying the antenna gains determined for one spectral line to other frequency bands. Another extension of self-calibration which is relevant at millimeter wavelengths is to determine the antenna gains from several nearby fields as in a mosaic observation. These options have been programmed into the MIRIAD software (Wright and Sault 1993), and have been used to good advantage to calibrate weak spectral line, or continuum emission using self-calibration on a strong spectral line which is observed simultaneously (e.g., Wright et al. 1995; Plambeck et al. 1995). For wide bandwidth multichannel observations (e.g., MFS synthesis, Conway et al. 1990), a further improvement to the self-calibration algorithm would be to determine the antenna gains as functions of the observing frequency, f , since the phase is expected to vary as $f\tau_w + f^{-2}\tau_i$, where τ_w is the tropospheric fluctuation (due mainly to water vapor), and τ_i is the ionospheric fluctuation. If the data contain simultaneous observations of millimeter and centimeter wavelengths, then the antenna gains can be used to determine both τ_w and τ_i . Even if the data are all at short wavelengths where the ionospheric delay is negligible, the fractional bandwidth may be quite large, and it would be better to scale the atmospheric delay with frequency, rather than apply the antenna phase directly over a wide frequency range.

4.9 Simultaneous Observation of Source and Calibrator

If the source is not strong enough for self-calibration on a time scale short compared with atmospheric phase fluctuations, another possibility is to simultaneously observe both the source and a nearby calibrator. This might be achieved by having a subset of the antennas observe the calibrator while the remaining antennas observe the source. Consider a pair of antennas, one looking at the source, the other at the calibrator. The effective separation between the source and the calibrator is given by $d = \sqrt{[h(s-s_0)]^2 + (b')^2}$ where b' is the baseline between these two antennas. After calibrating the source using the calibrator phase observed on the paired antenna, the phase fluctuation will be given by $D\phi(d)$; atmospheric phase fluctuations will be reduced if d is smaller than b , where b is the baseline being calibrated. Clearly, to work well the array configuration should consist of pairs of antennas with small separations compared with the baselines being used for the source observations. Using a smaller number of antennas to observe the calibrator increases d , and hence increases the residual phase fluctuations after calibration. Instrumental phase offsets between the antennas can be removed by alternating source and calibrator observations on

all antennas. The source and the calibrator need not be observed at the same frequency provided that the instrumental frequency response is properly accounted for in the calibration. A more detailed analysis of paired antenna configurations (assuming Taylor's hypothesis) is given by Holdaway (1992b). Since only half the array is used to observe the source at one time, the number of baselines [$N(N-1)/2$, where N is the number of antennas] is greatly reduced, and the paired antenna scheme is rather unattractive.

4.10 Measurements of Atmospheric Water Vapor

At millimeter wavelengths, both atmospheric emission and path-length variations are dominated by water vapor. Since the real and imaginary parts of the water-vapor refractivity are related through the Kramers-Kronig relation, we might be able to correct for the atmospheric path-length variations by measuring the atmospheric brightness fluctuations in the direction of the radio source. Near the 22.2 GHz water line the path-length variation with the brightness temperature of the emission is about 21 mm K^{-1} . The emission varies inversely with pressure, so that water vapor at high altitude causes less path-length change per K than at low altitude. At 20.6 GHz in the line wing, the path length per K brightness is nearly independent of the height of the water vapor (Westwater 1967; Thompson et al. 1986). Liquid water droplets in clouds also emit strongly, but cause little path-length change. Measurement of the brightness temperature at two or more frequencies enables estimates to be made of both water vapor and droplets. A JPL water-vapor radiometer at 20.7 and 31.4 GHz was able to determine the atmospheric path-length due to water vapor to 2.5 mm rms (Resch et al. 1984). The increased accuracy required for millimeter wavelength interferometry has led to renewed efforts to build better water-vapor radiometers at the 22 GHz water line at OVRO, and at 183 GHz at JCMT.

At an observing frequency away from the water lines, the emission from atmospheric water vapor is optically thin. In clear weather, assuming that all the water is in the form of water vapor, a measurement of the brightness temperature fluctuations gives a direct measurement of the integral, or column density, of water vapor in the direction of the radio source. The corresponding path-length variation is about 1.6 mm K^{-1} at 100 GHz, and 0.3 mm K^{-1} at 250 GHz (Welch 1994). Although the same receiver can be used for both observations and water-vapor measurements, the brightness temperature of the atmosphere must be measured to an accuracy of 0.01 K in order to measure 2 degrees of atmospheric phase shift at 100 GHz. For a typical (current) system temperature of 200 K, and a bandwidth of 1 GHz, the thermal noise allows this accuracy in an integration time 0.2 s, i.e., fast enough to follow the atmospheric fluctuations. However, the gain stability needed, 10^{-4} , requires careful attention to the thermal and mechanical stability of the receiver components, and the total powers on each antenna must be accurately calibrated (Plambeck et al. 1996). Two of the BIMA antennas were recently retro-fitted with receivers with the required gain stability. Figure 7 shows a plot of the phase and total-power difference between these two antennas during a test run with this new system. The phase and total-

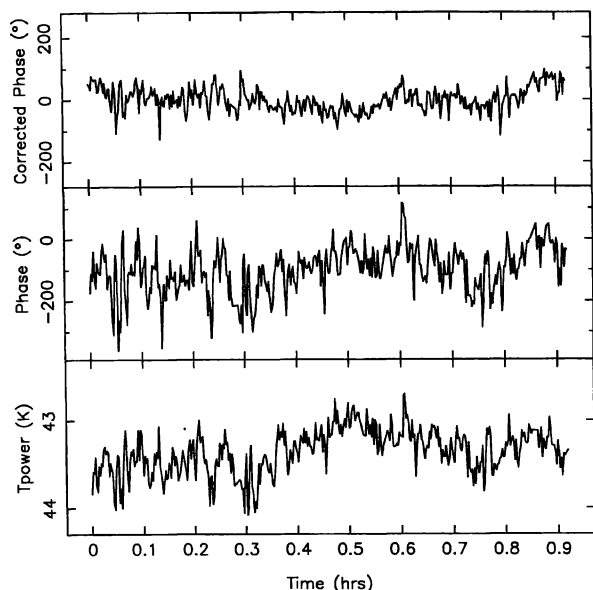


FIG. 7—Interferometer phase and total-power difference between two antennas separated by 43 m.

power fluctuations track closely with a correlation coefficient 0.86 (Fig. 8), and slope 2.5 mm K^{-1} , about 20 percent larger than the predicted value. Only an offset, corresponding to a difference in system temperature, has been removed from the total power since we wish to correct the phase using the total-power difference. There is little doubt that the total-power fluctuations correspond to atmospheric emission. The total-power fluctuations on each antenna are about 100 times larger on the sky than observed on an ambient temperature load, and each follows a structure function with time with a power-law slope $\beta=0.8$, consistent with our measured phase structure function. The two antennas were separated by only 43 m, and the total-power fluctuations on each antenna are nearly identical with a correlation coefficient 0.997. The total-power difference plotted in Fig. 7 does not perfectly track the interferometer phase. Correcting the interferometer phase by the measured atmospheric emission using the fitted slope, reduces the rms phase from 74 degrees to 34 degrees, a significant reduction in terms of the dynamic range in aperture synthesis images. The corresponding amplitude loss factor due to decorrelation, $e^{-\phi_{\text{rms}}^2}$, improves from 0.43 to 0.84. There are several possible reasons why the slope and the correlation might vary with atmospheric conditions. Since the slope (mm K^{-1}) varies with the altitude of the water vapor, multiple layers of turbulence at different altitudes will reduce the correlation between path length (phase) and emission. In particular, water vapor close to the ground, and close to the inversion layer may account for most of the turbulence (Lewellen 1980, see his Fig. 15). Aggregates of water vapor, dimers and polymers up to $n=10^6$ may cause variations in absorption up to 50 percent (Gebbie 1980). Thus it may be necessary to calibrate the slope of the correlation between path length and brightness temperature fluctuations (mm K^{-1}) quite often. This can be done from observations of a standard calibrator at intervals. There is also the

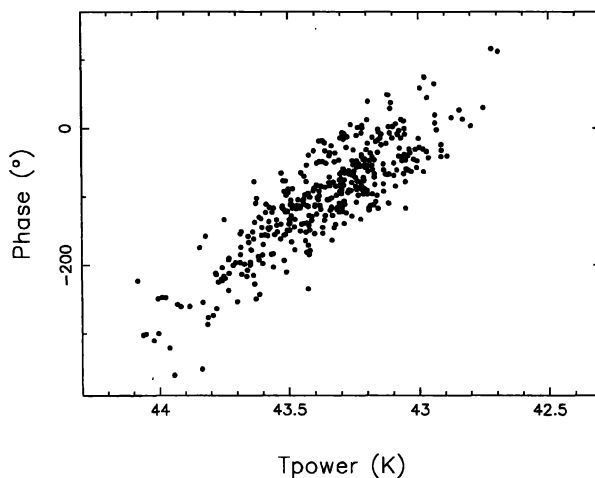


FIG. 8—Correlation between interferometer phase and total-power difference between two antennas separated by 43 m.

problem of interpolating the absolute system phase from the predicted atmospheric phase fluctuations which must be applied on times scale commensurate with the fluctuations, i.e., less than a few seconds, shorter than the usual integration and data dump times. One possible solution is to apply the predicted phase rate to each antenna from the measured emission change, dK/dt , and to calibrate the total system phase using the corrected average value of the calibrator phase which is observed at intervals. This procedure has the benefit of existing antenna hardware to set the phase rate (fringe rate generators and the like).

5. CONCLUSIONS

(1) Measurements of atmospheric phase fluctuations on a 1 km baseline show rms path-length variations of 1 mm on 10-s time scales at millimeter wavelengths. The standard phase calibration is inadequate; modified observing and data-reduction procedures are required for aperture synthesis at millimeter wavelengths on long baselines.

(2) The PSF follows a power law with slope $\beta=0.7$ in good weather, consistent with 2D turbulence. A β close to the Kolmogorov slope 1.67 for 3D turbulence is observed only on short baselines, and in turbulent weather. The variation of β , and the elevation dependence of the PSF suggest turbulent regions 100–300 m thick. Although similar rms and β are measured at other sites, there is evidence that the fluctuations decrease at high altitude under stable weather conditions.

(3) The measured rms phase can vary by factor 4, even in good weather—this requires flexible scheduling for efficient observing.

(4) Both rms and β increase with wind speed. The atmospheric phase fluctuations may be more closely associated with, and increase with, convective activity, rather than being in a frozen turbulent pattern transported over the array. At Hat Creek we have seen little direct evidence for any dependence of phase fluctuations with wind direction, and

derive an expression for combining temporal and spatial dependence in quadrature. Taylor's hypothesis for frozen water-vapor fluctuations may be more valid at other sites, but this remains to be demonstrated.

(5) Self-calibration techniques which remove the atmospheric phase fluctuations can greatly improve the data. At millimeter wavelengths a modified self-calibration to handle multiple channels and pointing centers is valuable, since the source flux density may not be concentrated in a few bright regions. Fitting atmospheric delay, rather than the phase, at each antenna is also desirable for wideband multi-channel and MFS synthesis. Although self-calibration is very successful for strong sources, it can lead to spurious results for weak sources with small arrays of antennas, and other methods of correcting for atmospheric phase fluctuations must be developed for aperture synthesis at millimeter wavelengths.

(6) Fast switching between a source and a nearby calibrator can reduce the rms phase on baselines longer than few hundred meters. Switching times of a few seconds are desirable but lead to high data rates for multichannel data.

(7) Predictions of the atmospheric delay from measurements of the atmospheric water-vapor emission show that it may be possible to correct the data in real time on short times scales. Further development of these techniques is needed.

(8) If a combination of fast phase switching, and phase correction from water-vapor measurements is able to correct for atmospheric phase fluctuations, so that phase coherent aperture synthesis images can be obtained using baselines of several km, then longer coherent integration times can also be used for millimeter VLBI, resulting in better sensitivity. Phase coherent VLBI images should also be possible with sub-milliarcsec resolution.

The Hat Creek array is operated by the Berkeley, Illinois, Maryland Association, supported in part by NSF Grant No. AST 93-20238. The author thanks the referee, Colin Masson, for many helpful comments, and for sharing his insights on corner frequencies and the like, Jack Welch, Don Backer, and Dick Plambeck for helpful conversations, and David Wilner for a careful reading of an early draft of the manuscript.

REFERENCES

- Altenhoff, W. J., Baars, J. W. M., Downes, D., and Wink, J. E. 1987, *A&A*, 184, 381
- Armstrong, J. W., and Sramek, R. A. 1982, *Radio Sci.*, 17, 1579
- Baldwin, J. E., and Wang Shouguan 1990, *IAU Symposium on Radio Astronomical Seeing* (Oxford, Pergamon)
- Bester, M., Danchi, W. C., Degiacomi, C. G., Greenhill, L. J., and Townes, C. H. 1992, *ApJ*, 392, 357
- Bieging, J. H., Morgan, J., Welch, W. J., Vogel, S. N., and Wright, M. C. H. 1984, *Radio Sci.*, 19, 1505
- Church, S. E., and Hills, R. E. 1990, *IAU Symposium on Radio Astronomical Seeing*, ed. J. E. Baldwin and Wang Shouguan (Oxford, Pergamon), p. 75
- Conway, J. E., Cornwell, T. J. and Wilkinson, P. N. 1990, *MNRAS*, 246, 490
- Coulman, C. E. 1991, *A&A*, 251, 743
- Coulman, C. E., and Vernin, J. 1991, *Appl. Opt.*, 30, 118
- Cornwell, T. J., and Fomalont, E. B. 1989, *Synthesis Imaging in Radio Astronomy*, ed. R. A. Perley, F. R. Schwab, and A. H. Bridle, *ASP Conf. Ser.*, 6, 185
- Davison, D. S. 1974, *Quart. J. Roy. Meteor. Soc.*, 100, 572
- Gebbie, H. A. 1980, in *Atmospheric Water Vapor*, ed. A. Deepak, T. D. Wilkerson, and L. H. Ruhnke (New York, Academic), p. 133
- Hinder, R., and Ryle, M. 1971, *MNRAS*, 154, 229
- Hinder, R. 1972, *J. Atm. Terr. Phys.*, 34, 1171
- Holdaway, M. A. 1991, *NRAO, Millimeter Array Memo*, 68
- Holdaway, M. A. 1992a, *NRAO, Millimeter Array Memo*, 84
- Holdaway, M. A. 1992b, *NRAO, Millimeter Array Memo*, 88
- Holdaway, M. A. 1995 *NRAO, Millimeter Array Memo*, preprint
- Holdaway, M. A., and Owen, F. N. 1995, *NRAO, Millimeter Array Memo*, 126
- Ishiguro, M., Kanazawa, T., and Kasuga, T. 1990, in *IAU Symposium on Radio Astronomical Seeing*, ed. J. E. Baldwin and Wang Shouguan (Oxford, Pergamon), p. 60
- Kaimal, J. C. 1974, *Quart. J. R. Meteorol. Soc.*, 100, 46
- Kaimal, J. C., and Finnigan, J. J. 1994, *Atmospheric Boundary Layer Flows* (Oxford, Oxford University Press)
- Kasuga, T., Kanzawa, T., and Ishiguro, M. 1986, *IEEE Trans. Antennas Propagation*, AP-34, 797
- Kasuga, T., Kanzawa, T., and Ishiguro, M. 1990, in *IAU Symposium on Radio Astronomical Seeing*, ed. J. E. Baldwin and Wang Shouguan (Oxford, Pergamon), p. 54
- Kolmogorov, A. N. 1941, *ANSSSR*, 30, 301
- Lewellen, W. S. 1980, in *Atmospheric Water Vapor*, ed. A. Deepak, T. D. Wilkerson, and L. H. Ruhnke (New York, Academic), p. 527
- Masson, C. R. 1994a, in *IAU on Very High Angular Resolution Imaging 1-10*, ed. J. G. Robertson and W. J. Tango
- Masson, C. R. 1994b, *Astronomy with Millimeter and Submillimeter Wave Interferometry*, ed. M. Ishiguro and Wm. J. Welch, *ASP Conf. Ser.*, 59, 87
- Olm, L., and Downes, D. 1992, *A&A*, 262, 634
- Plambeck, R. L., Wright, M. C. H., Mundy, L. G., and Looney, L. W. 1995, *ApJ*, 455, 189
- Plambeck, R. L., et al. 1996, in preparation
- Panofsky, H. A., and Dutton, J. A. 1984, *Atmospheric Turbulence* (New York, Wiley)
- Rogers, A. E. E., Moffet, A. T., Backer, D. C., and Moran, J. M. 1984, *Radio Sci.*, 19, 1552
- Rogers, A. E. E. 1988, *IAU Symposium 129*, p. 533
- Resch, G. M., Hogg, D. E., and Napier, P. J. 1984, *Radio Sci.*, 19, 411
- Sramek, R. A. 1983, *NRAO VLA Test Memo*, 143
- Sramek, R. A. 1990, in *IAU Symposium on Radio Astronomical Seeing*, ed. J. E. Baldwin and Wang Shouguan (Oxford, Pergamon), p. 21
- Tatarski, V. I. 1961, *Wave Propagation in a Turbulent Medium* (New York, McGraw-Hill)
- Taylor, G. I. 1938, *Proc. R. Soc. London A*, 164, 476
- Thompson, A. R., Moran, J. M., and Swenson, G. W., Jr. 1986, *Interferometry and Synthesis in Radio Astronomy* (New York, Wiley)
- Welch, W. J. 1994, *Astronomy with Millimeter and Submillimeter Wave Interferometry*, ed. M. Ishiguro and Wm. J. Welch, *ASP Conf. Ser.*, 59, 1
- Westwater, E. R. 1967, *ESSA Tech report, IER 30-ITSA 30*, Boulder, Colorado

Wilczak, J. M., and Businger, J. A. 1984, *J. Atmos. Sci.*, 41, 3551
Wright, M. C. H., and Welch, W. J. 1990, in *IAU Symposium on Radio Astronomical Seeing*, ed. J. E. Baldwin and Wang Shou-guan (Oxford, Pergamon), p. 71

Wright, M. C. H. 1991, BIMA memo 19 - Optimized Calibration
Wright, M. C. H., and Sault, R. J. 1993, *ApJ*, 402, 546
Wright, M. C. H., Plambeck, R. L., Mundy, L. G., and Looney, L. W. 1995, *ApJ*, 455, 185